Chalcogenide Letters

Tech Science Press

http://doi.org/10.32604/cl.2026.079634

ARTICLE

Structural and Optical Properties of $Cu_2ZnSn(S_{1-x}Se_x)_4$ Nanostructures Thin Film for Photovoltaic Applications

Bushra A. Hasan[1], Ameer J. Fadhl[2], Ahmad A. Hasan[1] and Yasser A. Jebbar[3,*]

[1]Department of Physics, College of Science, University of Baghdad, Baghdad, Iraq
[2]Department of Physics, College of Science, University of Kerbala, Karbala, Iraq
[3]AL-Mussaib Technical Institute, Al-Furat Al-Awsat Technical University, Babil, Iraq
*Corresponding Author: Yasser A. Jebbar. Email: yasser.jebbar.ims@atu.edu.iq

Received: 25 January 2026; Accepted: 19 March 2026; Published: 09 May 2026

ABSTRACT: Copper zinc tin sulfide selenide, $Cu_2ZnSn(S_{1-x}Se_x)_4$, absorbers are promising earth-abundant and environmentally benign materials for low-cost photovoltaic applications. This study investigates the structural and optical properties of $Cu_2ZnSn(S_{1-x}Se_x)_4$ nanostructured thin films prepared by pulsed laser deposition using melt-quenched targets with selenium compositions x = 0.0–1.0. X-ray diffraction revealed that films with low selenium content remained amorphous, whereas higher selenium incorporation promoted the formation of polycrystalline kesterite–stannite phases with preferred orientations along (112), (200), (220), and (312). The crystallite size increased from 12.3 to 17.9 nm as selenium reached x = 1.0, indicating enhanced crystal growth. Atomic force microscopy showed composition-dependent surface evolution, where average roughness decreased initially, reached a maximum of 88.29 nm at x = 0.6, and then declined, reflecting structural reorganization during phase transition. Optical characterization by UV–Vis–NIR spectroscopy demonstrated high absorption coefficients exceeding 10^4 cm^{-1} in the visible region, confirming strong light-harvesting capability. The direct optical band gap was tunable between 2.00 and 2.30 eV, with the highest value observed at x = 0.6 due to quantum confinement, nanoscale disorder, and compositional effects. The refractive index, extinction coefficient, and dielectric constants decreased with selenium addition up to x = 0.6, then increased at higher selenium contents, indicating a strong correlation between composition and optical response. The combined results highlight selenium control as an effective route for tailoring phase stability, transparency, and photon management for devices.

KEYWORDS: $Cu_2ZnSn(S_{1-x}Se_x)_4$ thin film; energy gap; dielectric constant; extinction coefficient; refractive index

1 Introduction

Chalcogenide thin-film photovoltaic technologies offer significant potential for the development of high-performance and large-area solar modules, enabling cost-effective and long-term solar energy harvesting [1–3]. Among them, $Cu(In,Ga)(S,Se)_2$ and CdTe solar cells have already achieved commercialisation, with power conversion efficiencies of approximately 12% and 20%, respectively [4–6]. However, the reliance on critical and toxic elements such as Cd, Ge, Te, and in limits their widespread application. In contrast, kesterite-based copper zinc tin sulfide (Cu_2ZnSnS_4) and its selenide counterpart are composed of earth-abundant and environmentally benign elements, making them highly attractive for scalable photovoltaic applications [7–10]. The structural and optical properties of $Cu_2ZnSn(S_{1-x}Se_x)_4$ are comparable to those of $Cu(In,Ga)(S,Se)_2$ and CdTe, while also offering non-toxicity and cost advantages. Despite these

benefits, the photovoltaic devices based on $Cu_2ZnSn(S_{1-x}Se_x)_4$ remain limited by relatively low conversion efficiencies (≤7%), high defect densities, bandgap mismatch, and phase inhomogeneity [11–14]. Various deposition techniques have been explored, including sputtering, thermal co-evaporation, electrodeposition, and solution-based nanocrystal inks. While vacuum-based methods allow precise control of composition and phase, they require significant energy and cost, suffer from low material utilisation, and often show limited throughput [15]. To overcome these limitations, pulsed laser deposition and alternative synthesis strategies have been proposed. Recently, we reported a simple and low-cost route to prepare copper zinc tin sulfide selenide targets for laser ablation by heating elemental powders at the eutectic temperature without the use of hazardous solvents or organic additives [16]. Although the initial device efficiency achieved with this method was modest (≈5.1%), the approach demonstrates the feasibility of producing absorber layers with reduced toxicity and cost [16]. In this study, the structural and optical properties of copper zinc tin sulfide selenide thin films are systematically investigated. The films were characterised using X-ray diffraction (XRD), atomic force microscopy, and ultraviolet–visible–near infrared (UV-Vis-NI) spectroscopy to better understand their phase evolution, morphology, and band gap characteristics, thereby addressing the efficiency-limiting factors observed in earlier reports.

2 Experimental Procedure

$Cu_2ZnSn(S_{1-x}Se_x)_4$ alloys were fabricated by the quenching technique, a nontoxic process, as presented in our previous studies [17,18]. The demand amount of high purity (99.999%) (Cu, Zn, Sn, S, and Se) elements supplied from Sigma Aldrich Co., St. Louis, in accordance with their atomic percentages for different Se content in the range (x = 0.0, 0.2, 0.4, 0.6, 0.8, and 1.0), was weighed using an electronic balance with the least count of (10^{-4} g). The mixed elements were sealed in an evacuated (~10^{-3} Torr) quartz ampoule. The ampoules containing the elements were heated to 900°C for 12 h and then cooled to room temperature. The temperature of the furnace was raised at a rate of 10°C/min. During heating the ampoules are constantly rocked. This was done to obtain homogeneous glassy alloys. The extracted materials were ground and processed into pellet shapes to be used as targets for laser ablation. $Cu_2ZnSn(S_{1-x}Se_x)_4$ thin films of different Se content were prepared using the pulsed laser deposition method as shown in Fig. 1. An Nd:YAG laser beam (with energy, pulsed, and frequency of 0.4 J, 350, and 6 Hz, respectively) was used to do the deposition in a 2×10^{-2} Torr. A window allowed the laser beam to focus on the target.

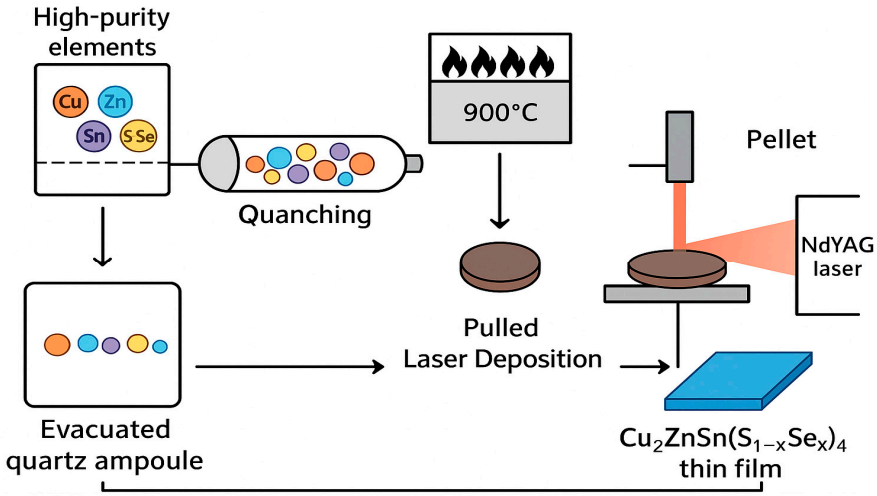

Figure 1: Schematic representation of experimental procedure of the present work.

The thin films were formed by ablated atoms impacting on glass substrates, and the following equation provides the film thickness (t) [19]:

$$t = \frac{\lambda \Delta x}{2x} \tag{1}$$

where λ is the X-ray wavelength and Δx and x are the shift between interference fringes, the distance between the interference fringes, respectively.

The crystal structure of $Cu_2ZnSn(S_{1-x}Se_x)_4$ alloys and thin films after annealing at a temperature of 300°C was carried out using XRD with CuKα radiation (λ = 1.5406 Å). The average crystal size (D) using Scherrer's formula and strain (ε') of the prepared thin films were conducted when full width at half maximum is known using the following equations [20]:

$$D = \frac{K\lambda}{\beta \cos\theta} \tag{2}$$

$$\varepsilon' = \frac{\beta}{(4 \tan\theta)} \tag{3}$$

where K is the so-called Scherrer constant it can have values anywhere from 0.62 and 2.08 (in this work, K = 0.9 was used), β is the width of the X-ray peak on the 2θ axis normally measured as full width at half maximum (FWHM) after the error due to instrumental broadening has been properly corrected (subtraction of variances), and θ is the Bragg angle. The average roughness of $Cu_2ZnSn(S_{1-x}Se_x)_4$ thin films has been measured using the AFM. A Shimadzu UV-1800, a UV-visible spectrophotometer manufactured in Japan, was used to perform the optical measurements. The gadget used wavelengths in ranging 190–1100 nm to measure the transmittance and absorbance spectra of the $Cu_2ZnSn(S_{1-x}Se_x)_4$ thin films that have been manufactured. The following equation is used to determine the absorption coefficient [21]:

$$\alpha = \frac{2.303A}{t} \tag{4}$$

where A is the absorbance. The Tauc relation for direct allowed transitions is used to measure the optical energy gap:

$$(\alpha h\nu)^2 = C\left(h\nu - E_g\right) \tag{5}$$

where h is the blank's constant, ν is the frequency of X-ray radiation, C is proportionality constant, and E_g is the band gap energy. The following equations are used to calculate the optical constants, including the extinction coefficient (k), the refractive index (n), and the real (ε_r) and imaginary (ε_i) parts of the dielectric constants [22]:

$$k = \frac{\alpha\lambda}{4\pi} \tag{6}$$

$$n = \sqrt{\frac{(1+k)^2}{(1-k)^2} - (k^2 - 1)} + \frac{(1+R)}{(1-R)} \tag{7}$$

$$\varepsilon_r = n^2 - k^2 \tag{8}$$

$$\varepsilon_i = 2nk \tag{9}$$

3 Results and Discussion

3.1 Structural Analysis

The XRD was used to characterize the identified structural phase of the synthesized powders. Fig. 2 declared the diffraction pattern of the fabricated $Cu_2ZnSn(S_{1-x}Se_x)_4$ powders. It was clear that increasing the Se content from 0% to 100% converted the phase gradually from kesterite Cu_2ZnSnS_4 to stannite $Cu_2ZnSnSe_4$, as appeared from the gradual shift of diffraction peaks to lower angle values. This shift is ascribed to the expansion of the interplanar spacing as a result of introducing bigger Se atoms. The diffraction pattern is free from any additional secondary phases. Also, the XRD data for $Cu_2ZnSn(S_{1-x}Se_x)_4$ powders are listed in Table 1.

The uncertainty in the crystallite size (ΔD) was calculated using the following error propagation equation:

$$\Delta D = D\sqrt{\left(\frac{\Delta\beta}{\beta}\right)^2 + (\tan\theta\Delta\theta)^2} \tag{10}$$

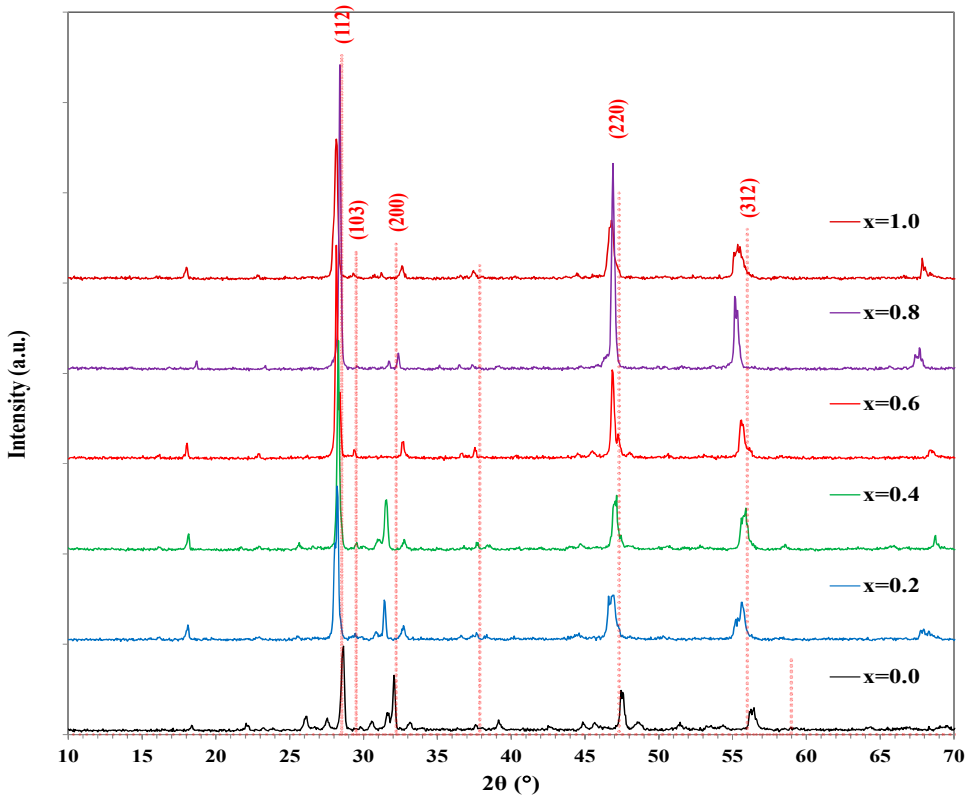

Figure 2: XRD patterns for $Cu_2ZnSn(S_{1-x}Se_x)_4$ powders.

Table 1: XRD data for $Cu_2ZnSn(S_{1-x}Se_x)_4$ powders.

x	2θ (°)	β (°)	d_{hkl} (Å)	$D_{Scherrer}$ (nm)	ε'	hkl
0.0	28.63	0.24	3.11	33.0 ± 1.5	0.004	(112)
	32.03	0.30	2.79	27.3 ± 1.0	0.005	(200)
	47.52	0.33	1.91	26.3 ± 0.8	0.003	(220)
	56.32	0.52	1.63	17.2 ± 0.3	0.004	(312)
0.2	28.19	0.33	3.16	24.8 ± 0.8	0.006	(112)
	32.61	0.41	2.74	20.0 ± 0.5	0.006	(200)
	46.86	0.57	1.93	15.0 ± 0.3	0.006	(220)
	55.63	0.49	1.65	18.1 ± 0.4	0.004	(312)
0.4	28.28	0.22	3.15	37.2 ± 1.8	0.004	(112)
	32.72	0.38	2.73	21.5 ± 0.6	0.006	(200)
	47.11	0.35	1.92	24.2 ± 0.7	0.004	(220)
	55.82	0.52	1.64	17.2 ± 0.3	0.004	(312)
0.6	28.14	0.22	3.16	37.1 ± 1.8	0.004	(112)
	32.66	0.27	2.73	30.0 ± 1.2	0.004	(200)
	46.86	0.27	1.93	31.4 ± 1.3	0.003	(220)
	55.57	0.35	1.65	25.1 ± 0.8	0.003	(312)
0.8	28.39	0.22	3.14	37.2 ± 1.8	0.004	(112)
	32.33	0.22	2.76	37.5 ± 1.9	0.003	(200)
	46.89	0.27	1.93	31.4 ± 1.3	0.003	(220)
	55.24	0.33	1.66	27.1 ± 0.9	0.003	(312)
1.0	28.14	0.27	3.16	29.7 ± 1.2	0.005	(112)
	32.58	0.33	2.74	25.0 ± 0.8	0.005	(200)
	46.72	0.41	1.94	20.9 ± 0.5	0.004	(220)
	55.33	0.66	1.65	13.6 ± 0.2	0.006	(312)

Fig. 3 displays the XRD pattern of $Cu_2ZnSn(S_{1-x}Se_x)_4$ thin films. The prepared thin films with low Se content showed amorphous structures, i.e., the XRD pattern is free from any diffraction peaks. By increasing Se content to x of 0.8, the structure is converted to polycrystalline with nanostructure. It is observed that the formation of crystalline quaternary semiconductor. The observed peaks of the $Cu_2ZnSn(S_{1-x}Se_x)_4$ nanostructure film at 2θ = 28.45°, 32.12°, and 47.30° coincided with the diffraction of the (112), (200), and (220) planes of $Cu_2ZnSn(S_{1-x}Se_x)_4$ (JCPDS No. 26-0575) [23], respectively, which clearly reflects the stannite structure of $Cu_2ZnSnSe_4$. In the case of the selenides $Cu_2ZnSnSe_4$, the 2θ values of the major peaks of the (112), (200), and (220) planes were shifted toward lower angles due to the larger unit cell lattice parameters of the $Cu_2ZnSn(S_{1-x}Se_x)_4$ with S sufficiently replaced by Se. Additionally, the existence of secondary phases was indicated by the detection of a novel peak at 2θ of 29.57°. These phases would be near phase-pure CZTS and/or less Se-replaced $Cu_2ZnSn(S_{1-x}Se_x)_4$. They are either separated or dispersed across the Se-rich $Cu_2ZnSn(S_{1-x}Se_x)_4$ film. The peaks seen at 2θ of 56.24° in Fig. 3 correspond to the (312) crystal orientation, which is indexed to stannite $Cu_2ZnSnSe_4$ (JCPDS 52-0868) [22,24] based on XRD data.

The peak at 29.57° which is indexed as (103) (JCPDS 52-0868), it confirms the structural ordering of the kesterite $Cu_2ZnSn(S_{1-x}Se_x)_4$ phase. It belongs to the main absorber material itself, not a secondary phase, assuming it is part of the characteristic diffraction pattern of the CZTSSe thin film [25]. The average crystallite size had been estimated to be 12.3 ± 0.2 nm using the Scherer equation under the assumption of spherical nanoparticles, increasing to 17.9 ± 0.4 nm by increasing the Se content to 100%, as presented in Table 2.

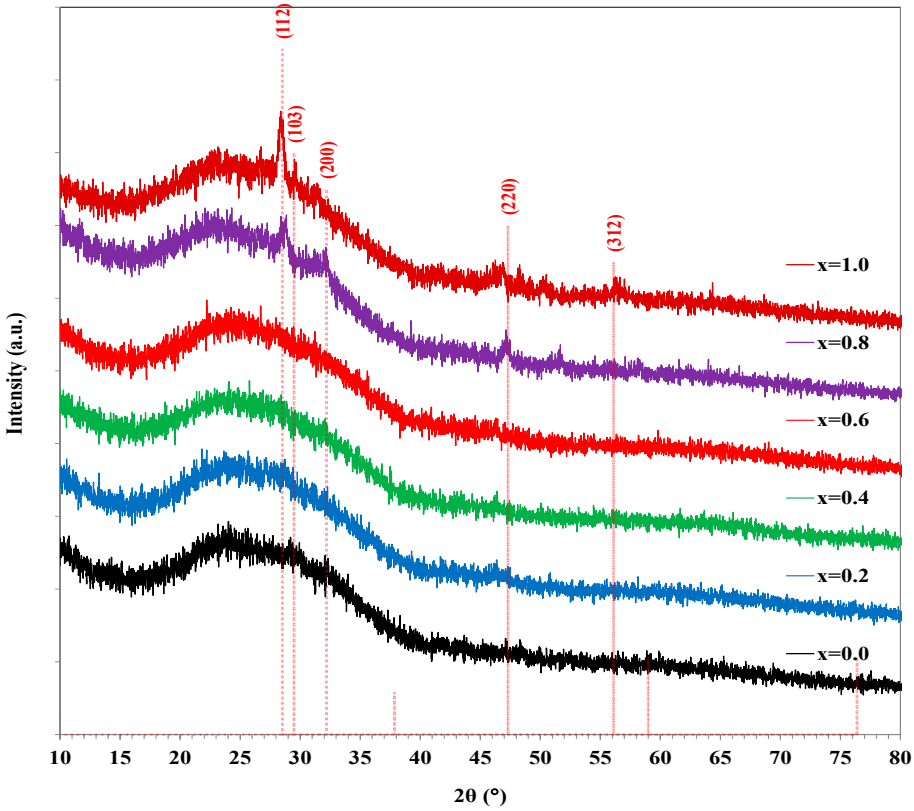

Figure 3: XRD patterns for $Cu_2ZnSn(S_{1-x}Se_x)_4$ nanostructures thin films.

Table 2: XRD data for $Cu_2ZnSn(S_{1-x}Se_x)_4$ nanostructures thin films.

x	2θ (°)	β (°)	d_{hkl} (Å)	$D_{Scherrer}$ (nm)	ε'	hkl
0.0	Amorphous					
0.2	Amorphous					
0.4	Amorphous					
0.6	Amorphous					
0.8	28.49	0.66	3.13	12.3 ± 0.2	0.011	(112)
	32.12	0.58	2.78	14.2 ± 0.3	0.009	(200)
	47.14	0.70	1.92	12.2 ± 0.2	0.007	(220)
1.0	28.36	0.45	3.14	17.9 ± 0.4	0.008	(112)
	29.57	0.41	3.01	19.7 ± 0.5	0.007	(103)
	31.49	0.58	2.83	14.1 ± 0.3	0.009	(200)
	46.94	0.58	1.93	14.8 ± 0.3	0.006	(220)
	56.24	0.58	1.63	15.4 ± 0.3	0.005	(312)

3.2 AFM Measurements

The values of average roughness and average diameter from the AFM are shown in Fig. 4. It was obvious that the average roughness gets to decrease by increasing the Se content up to x of 0.4, then it grows up suddenly at x of 0.6 to reach its maximum value of 88.29 nm and drop again. The roughness is usually related to the absorption of the incident light, i.e., a rougher surface means more absorption of the

incident light. The average diameter gets to grow up irregularly by increasing the Se content, as in Table 3; this result is consistent with the results obtained from XRD.

While it is true that for many materials (especially metals), increased roughness leads to multiple reflections/scattering, which traps light and increases absorption, the relationship is complex and depends heavily on the wavelength, material, and type of roughness. Here is a breakdown of when roughness increases vs. decreases absorption: When Roughness Increases Absorption: (i) Multiple Reflections/Light Trapping: Surface features (grooves, bumps) allow light to bounce multiple times, increasing the probability of absorption before escaping. (ii) Surface Area Increase: A rougher surface has more surface area, which can increase absorption. (iii) Reduced Specular Reflection: Roughness breaks up the specular (mirror-like) reflection, reducing the amount of light that reflects directly away. (iv) X-Ray/Grazing Incidence: For grazing incidence mirrors, roughness can drastically increase absorption.

Also, when roughness can decrease absorption our special, this take place occurs when: (i) Increased Backscattering: If the roughness causes a high amount of light to be scattered backward (backscattered) away from the material, it can lead to a lower total absorption. (ii) Wavelength/Structure Mismatch: If the surface roughness (correlation length) is not optimal, it may scatter light away rather than into the material. (iii) Left-Handed Materials (LHMs): In certain engineered materials, increased roughness can significantly reduce absorption, contrary to normal materials. (iv) Particle/Surface Type: For certain polymeric surfaces, increased roughness has been shown to reduce surface absorption.

In summary, while roughing a surface is a common technique to increase absorption (e.g., in solar cells or laser welding), it is not a universal rule. The effect of surface roughness is highly dependent on the RMS roughness height and the correlation length of the surface features relative to the wavelength of the light [26].

3.3 The Optical Measurements

Following the examination of the structural characteristics of $Cu_2ZnSn(S_{1-x}Se_x)_4$, the optical parameters of the thin films were determined by calculating the reflectance (R) and transmission (T) spectra. Figs. 5 and 6 show the R and T spectra of $Cu_2ZnSn(S_{1-x}Se_x)_4$ thin films at wavelength (λ) between 300 and 1100 nm. According to these figures, the T of $Cu_2ZnSn(S_{1-x}Se_x)_4$ thin films in the visible wavelength region 400–700 nm had 20–80% values, while the spectrums of R and T of $Cu_2ZnSn(S_{1-x}Se_x)_4$ thin films at 700–1000 nm were approximately constant. The values of R and T did not significantly alter in a large geographical range (beyond roughly 500 nm). The R and T spectra of $Cu_2ZnSn(S_{1-x}Se_x)_4$ thin films were essential for comprehending their optical characteristics, which were essential for many optoelectronic uses such as light-emitting devices, photovoltaics (solar cells), and photodetectors. Additionally, the R and T spectra were essential for describing the optical characteristics of $Cu_2ZnSn(S_{1-x}Se_x)_4$ thin films because they offer important information on their band gap, absorption patterns, reflection losses, and optical constants. Optimising the efficiency of photovoltaic devices and other optoelectronic applications employing $Cu_2ZnSn(S_{1-x}Se_x)_4$ thin films requires this knowledge.

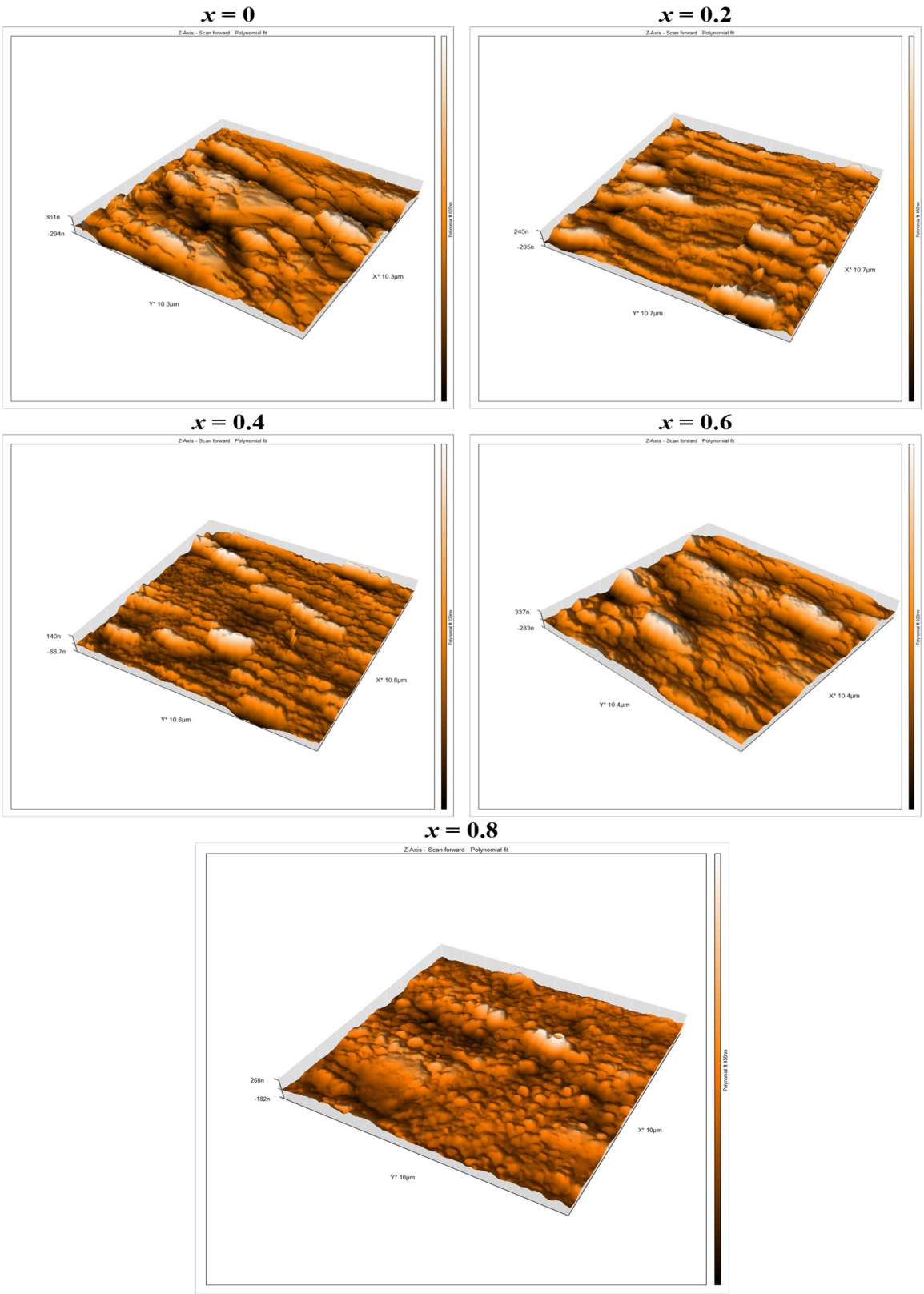

Figure 4: Images of $Cu_2ZnSn(S_{1-x}Se_x)_4$ nanostructures thin films.

Table 3: AFM data for $Cu_2ZnSn(S_{1-x}Se_x)_4$ nanostructures thin films.

x	Average Diameter (nm)	Average Roughness (nm)
0.0	65.85	103.40
0.2	92.54	55.61
0.4	65.84	27.48
0.6	84.65	88.29
0.8	96.54	62.18
1.0	-	-

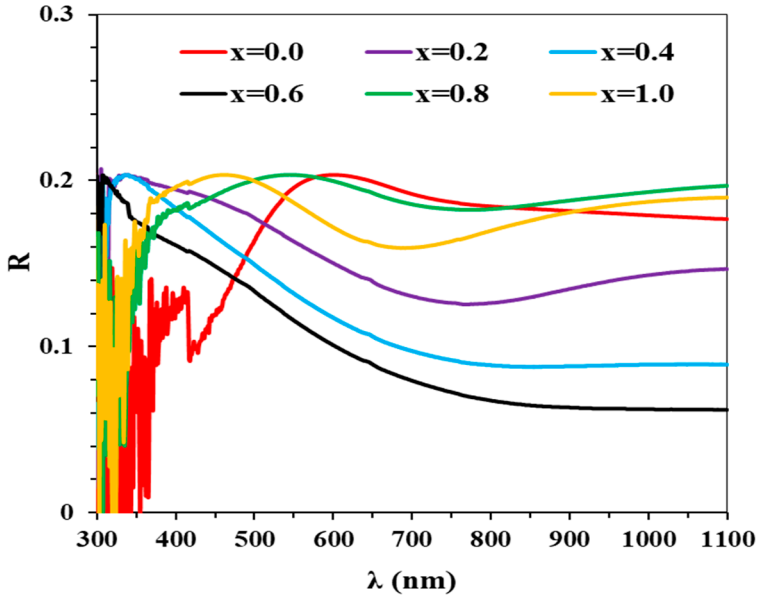

Figure 5: Reflectance (*R*) spectra of $Cu_2ZnSn(S_{1-x}Se_x)_4$ nanostructures thin films with x = 0.0, 0.2, 0.4, 0.6, 0.8, and 1.0.

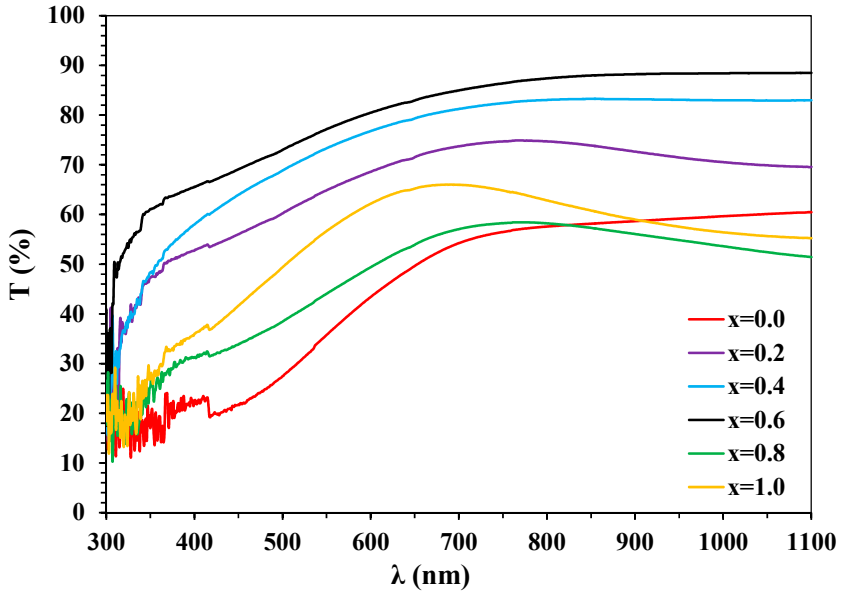

Figure 6: Transmittance (*T*) spectra of $Cu_2ZnSn(S_{1-x}Se_x)_4$ nanostructures thin films with x = 0.0, 0.2, 0.4, 0.6, 0.8, 1.0.

Fig. 7 shows the variation of the absorption coefficient (α) for $Cu_2ZnSn(S_{1-x}Se_x)_4$ nanostructure films with wavelength (λ). It was obvious that α is greater than 10^4 cm^{-1} for the visible near-infrared region. The highest α value means that this material will absorb a greater fraction of incident light, which is important for maximising the photovoltaic efficiency, as higher absorption leads to a greater generated electrical current. There are several reasons for the notably significant absorption of $Cu_2ZnSn(S_{1-x}Se_x)_4$ nanostructure films in the low wavelength region, including the band gap energy, the impact of quantum confinement, composition, defects, and morphology. $Cu_2ZnSn(S_{1-x}Se_x)_4$ is a tunable band gap semiconductor material nanocrystal. It is well known that nanostructures have a high surface-to-volume ratio, and surface states act as centers for additional absorption in the high-energy side or low wavelength region. The quantum confinement as well as another effects which will explained below leads to absorption of light in the high-energy region, which gives rise to band gap broadening. The broadening occurring in the optical energy gap can be explained by several factors besides quantum confinement (size-dependent effects), which are common in thin films and engineered chalcogenides (like Cu_2ZnSnS_4/Se) as in the following. (i) Structural Defects and Stoichiometry Changes: A higher bandgap is often caused by a large density of defects or deviations from the ideal stoichiometry (e.g., changes in the ratio of Cu/Zn/Sn/S/Se). (ii) Compositional Variation (Substitution): If the composition changed during fabrication—such as substituting Zinc with smaller atoms (e.g., larger alkali-earth metals, although Ba/Sr substitution usually reduces the gap, substitution with smaller atoms generally increases it) or increasing Sulfur content in selenide films—the lattice constant changes, leading to a wider bandgap. (iii) Surface Defects and Strain: For thin films, surface-to-volume ratios are high. Surface atoms often have different coordination, and if the film is under compressive strain due to substrate mismatch, it can widen the bandgap. (iv) Oxidation: If the films are exposed to air, the formation of surface oxides (e.g., ZnO, SnO_2) on top of the sulfide/selenide can show a higher effective bandgap in optical measurements, and finally (v) Amorphous Nature/Disorder: The presence of a high degree of amorphousness or structural disorder in the thin films can lead to band-tailing, which often increases the measured optical bandgap [23].

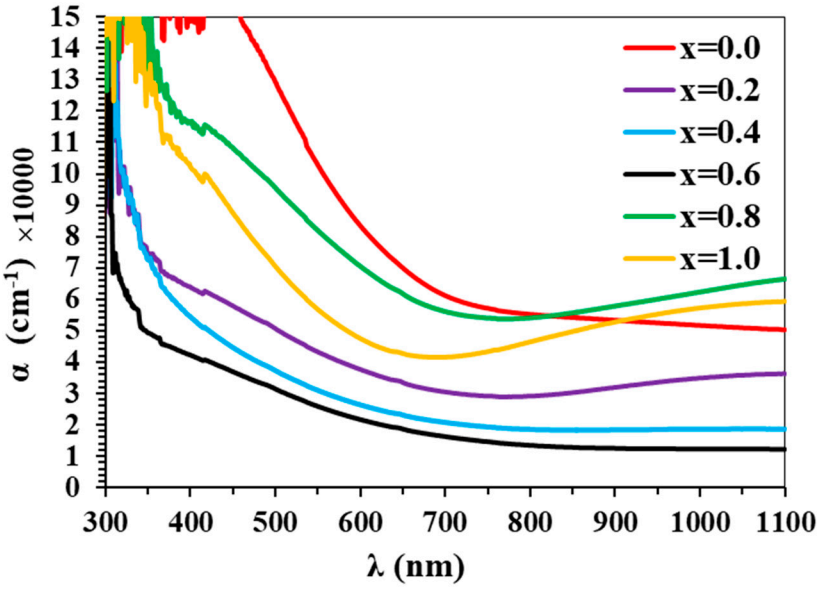

Figure 7: Variation of the absorption coefficient (α) with wavelength (λ) for $Cu_2ZnSn(S_{1-x}Se_x)_4$ nanostructure films with x = 0.0, 0.2, 0.4, 0.6, 0.8, and 1.0.

To investigate the band gap energy (E_g) of the $Cu_2ZnSn(S_{1-x}Se_x)_4$ nanostructure thin films, it is important to calculate the variation of $(\alpha h\nu)^2$ with $(h\nu - Eg)$ and draw its results as shown in Fig. 8. The E_g was obtained from determining the linear portion of the plot $(\alpha h\nu)^2$ against photon energy ($h\nu$). The E_g values for $Cu_2ZnSn(S_{1-x}Se_x)_4$ nanostructure thin films were ≅2.10, 2.05, 2.20, 2.30, 2.00, and 2.05 eV for x of 0.0, 0.2, 0.4, 0.6, 0.8, and 1.0, respectively, as shown in Table 4. It can be observed that there was no significant difference between the E_g of Cu_2ZnSnS_4 ≅ 2.10 eV) and $Cu_2ZnSnSe_4$ (≅2.05 eV). In order to compare our result with the published data, a significant E_g between Cu_2ZnSnS_4 (1.51 eV) and $Cu_2ZnSnSe_4$ (1.24 eV) and it was observed that the E_g for Cu_2ZnSnS_4 was higher than for $Cu_2ZnSnSe_4$. This is attributed to the difference in electronegativity (the S has a larger electronegativity than the Se) as well as the difference in atomic size between the S and the Se. Hence, in $Cu_2ZnSnSe_4$, the Se with 4p orbitals was more spread out than the S with 3p orbitals in Cu_2ZnSnS_4. The Se atoms are larger than S atoms; this structural difference enables stronger orbital overlap with the Cu and Sn d-orbitals, which consequently reduces the E_g of $Cu_2ZnSnSe_4$ compared with Cu_2ZnSnS_4 [27]. For instance, CZTS films prepared by co-evaporation and spray pyrolysis exhibited E_g of 1.45 eV and 1.48 eV, respectively [28], while the systematic variation from 1.51 eV to 1.24 eV had been reported with increasing Se incorporation [1]. This clear band gap narrowing highlights the tenability of $Cu_2ZnSn(S_{1-x}Se_x)_4$ alloys through compositional engineering. The E_g, together with factors such as quantum confinement, composition, defects, and morphology, contributes to the strong absorption of CZTSSe nanostructured films in the visible to near-infrared spectral range [27]. Tauc analysis reveals a single direct optical transition without additional absorption shoulders, confirming that the optical band gap values (2.0–2.03 eV) are predominantly governed by the CZTSSe phase. The observed direct band gap values (2.00–2.30 eV) are higher than the typical range reported for bulk CZTSSe (1.0–1.5 eV). Quantum confinement effects are likely to be the dominant factor, as the crystallite sizes derived from XRD was increases 12.3 ± 0.2 nm to 17.9 ± 0.4 nm within the confinement regime.

For more explanation the high energy gap values can be explained as follows: The bandgap of a material in its crystalline form is determined by its lattice constant and its dielectric constant. Specifically, it is inversely proportional to the interatomic distance and the dielectric constant.

Then if one reduces the size of crystal to be in form of crystallite will nanometer size, The electrons in the crystallites will be confined in this small volume leading to the quantization of the electron levels in the conduction band and hole levels in the valence band. This will lead to the shift of the band edges far from each others causing the increase of the energy gap as the crystallite size decreases [28].

The broadening occurring in the optical energy gap at high selenium content facilitates the compound's use as a window. From a photovoltaic perspective, such widened band gaps reduce visible-light absorption and therefore limit their suitability as single-junction absorber layers, though they may be beneficial for window or tandem applications.

Although thin films remain amorphous or partially crystalline up to x = 0.6, the presence of nanoscale crystalline domains within the amorphous matrix can still contribute to light absorption and carrier generation. Moreover, amorphous films have been shown in other semiconductor systems to produce photo-response when suitably engineered with mixed phases. Upon post-deposition annealing in a controlled Se/S atmosphere, improved crystallinity, increased grain size, and enhanced carrier transport are expected—standard steps in kesterite absorber processing that significantly improve photovoltaic properties. This plan for annealing is aligned with approaches used in recent literature to reduce defect densities and enhance crystal quality, thereby increasing suitability of the films as photovoltaic absorber layers [29,30].

On the other hand the relationship between thickness and energy gap (band gap) in materials, particularly in thin-film semiconductors and nanomaterials, is generally inverse: as the thickness of

a material decreases, the energy gap increases. Conversely, increasing the thickness typically results in a decrease in the energy gap. Thus the high value of energy gap are attributed to low thickness since the prepared thin films were thicknes of 150 nm.

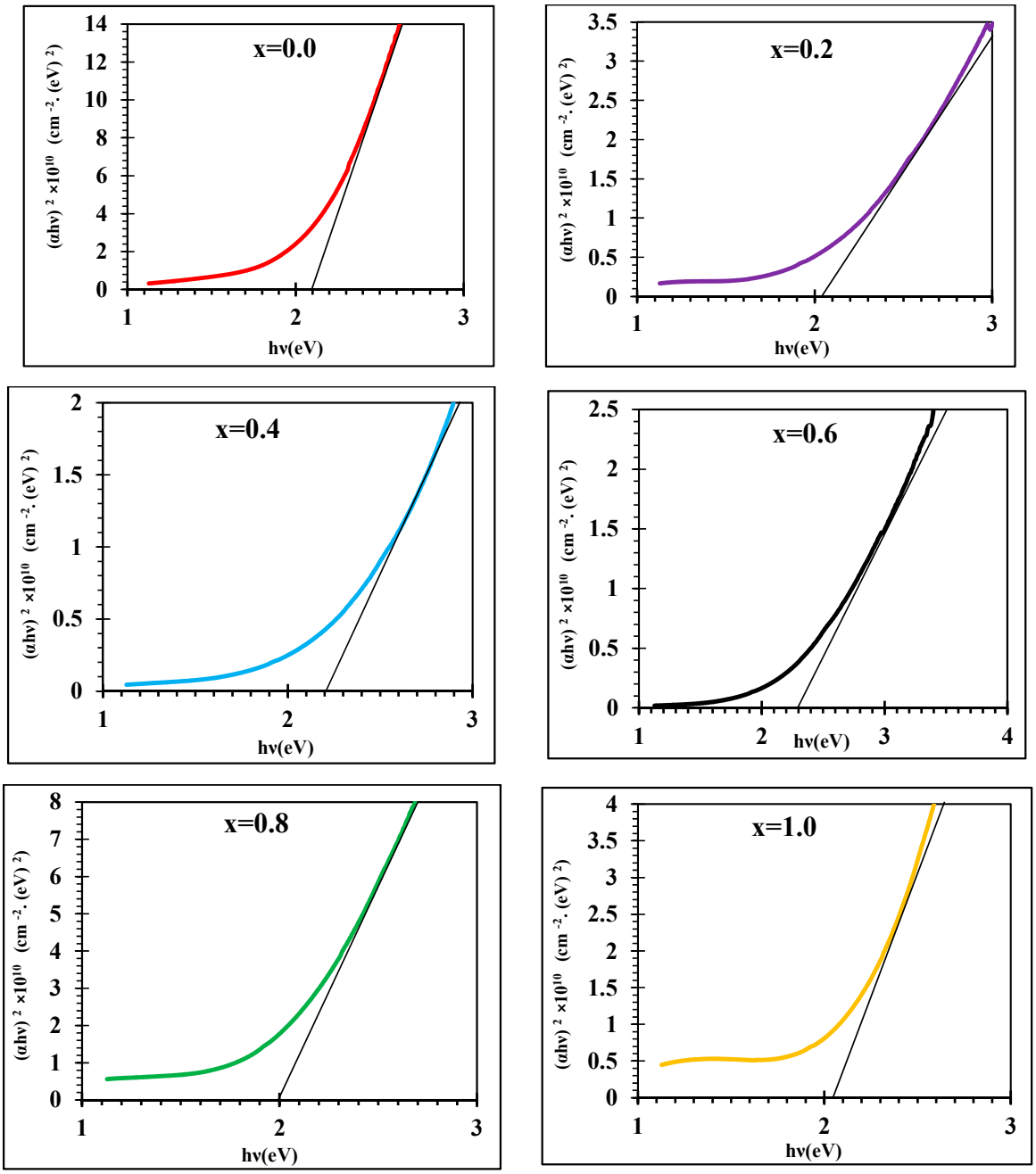

Figure 8: Variation of $\alpha h\nu$ with photon energy ($h\nu$) for $Cu_2ZnSn(S_{1-x}Se_x)_4$ nanostructures thin films with x = 0.0, 0.2, 0.4, 0.6, 0.8, and 1.0.

Table 4: The values of the optical parameters and E_g at wavelength of 550 nm for $Cu_2ZnSn(S_{1-x}Se_x)_4$ nanostructures thin films.

x	T (%)	α (cm^{-1})	k	n	ε_r	ε_i	E_g (eV)
0	35.7	102,829	0.45	2.58	6.49	2.33	2.1
0.2	64.8	43,296	0.19	2.35	5.51	0.89	2.05
0.4	73.3	31,033	0.13	2.14	4.56	0.58	2.20
0.6	77.1	25,909	0.11	2.03	4.11	0.46	2.3
0.8	44.0	81,987	0.35	2.64	6.85	1.89	2
1.0	56.6	56,827	0.24	2.52	6.29	1.25	2.05

The extinction coefficient (k) spectrum of $Cu_2ZnSn(S_{1-x}Se_x)_4$ nanostructure thin films is depicted in Fig. 9. The k increased monotonically as the λ increased. The k decreased from 0.45 to 0.11 by increasing the Se content from 0.0 to 0.6, while it increased with further increase of the Se content in the mentioned range. This behaviour is attributed to a reduction of the α taking place as a result of increasing the Se content in the mentioned range. It was observed that in Cu_2S thin films annealed at different temperatures, the k decreased from 0.023 at 27°C to 0.016 at 100°C before sharply increasing to 0.072 at 200°C. This behaviour was attributed to the reduction of α with increasing Se content, followed by the sudden increase due to structural reorganisation at higher thermal treatments [30–34].

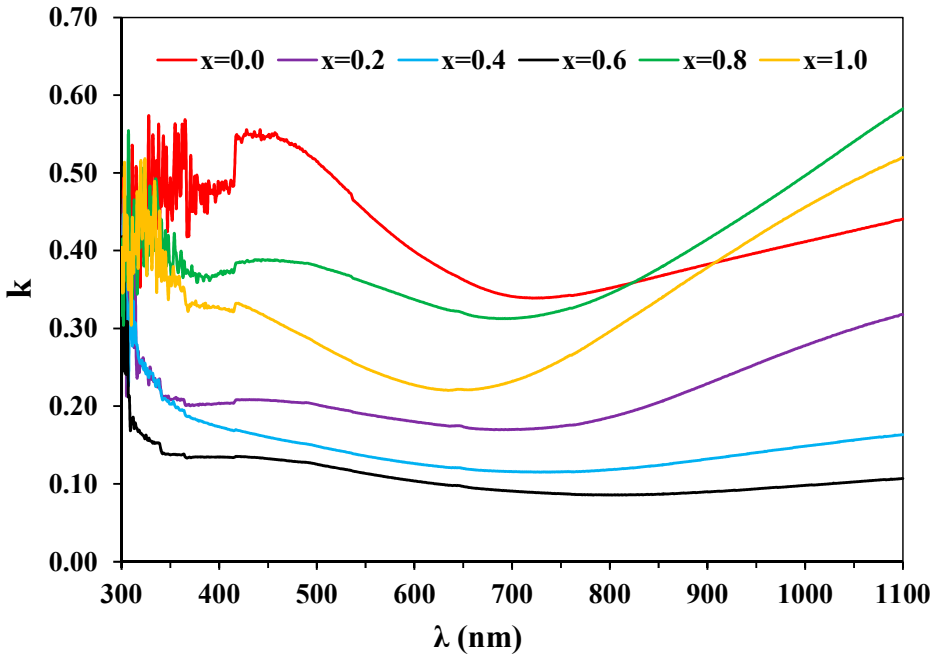

Figure 9: Variation of extinction coefficient (k) with wavelength (λ) for $Cu_2ZnSn(S_{1-x}Se_x)_4$ nanostructures thin films with x = 0.0, 0.2, 0.4, 0.6, 0.8, and 1.0.

The variation of refractive index (n) with wavelength (λ) is plotted in Fig. 10. It was noted that the value of n changed from 2.58 to 2.03. The reduction of n was attributed to the increasing transparency of the synthase thin films, which consequently led to an increase in the velocity of light in this medium [35,36].

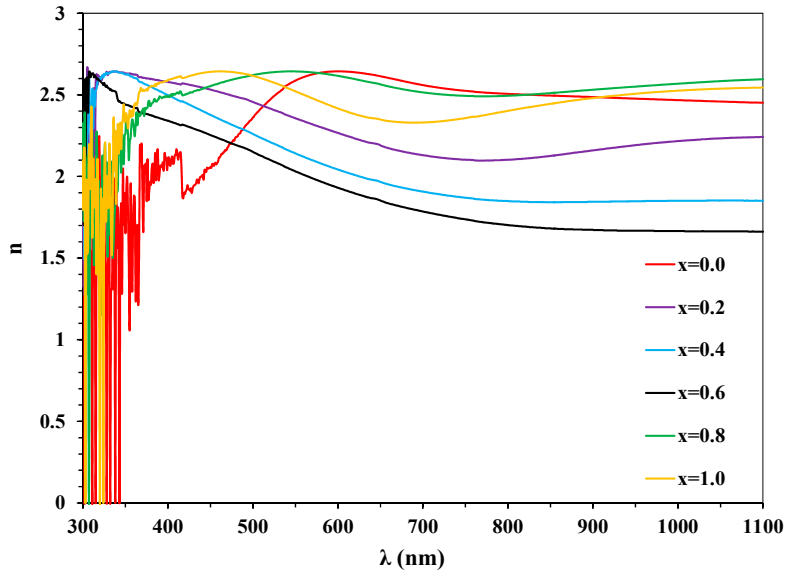

Figure 10: Variation of refractive index (n) with wavelength (λ) for $Cu_2ZnSn(S_{1-x}Se_x)_4$ nanostructures thin films with x = 0.0, 0.2, 0.4, 0.6, 0.8, and 1.0.

Moreover, one of material's optical characteristics is its complicated dielectric function. The real part (ε_r) and the imaginary part (ε_i) make up the complex dielectric function. The ε_r and ε_i are dependent on the k and n of the material. The changes in ε_r and ε_i with λ are shown in Figs. 11 and 12, respectively. According to these figures, at λ = 550 nm, the values of ε_r and ε_i decreased from 6.49 to 4.11 and from 2.33 to 0.46, respectively, when the Se content increased from 0.0 to 0.6. On the other hand, it was obvious that the ε_r behaviour trend was quite similar to the n graph, while the behaviour trend of ε_i was quite similar to the k graph.

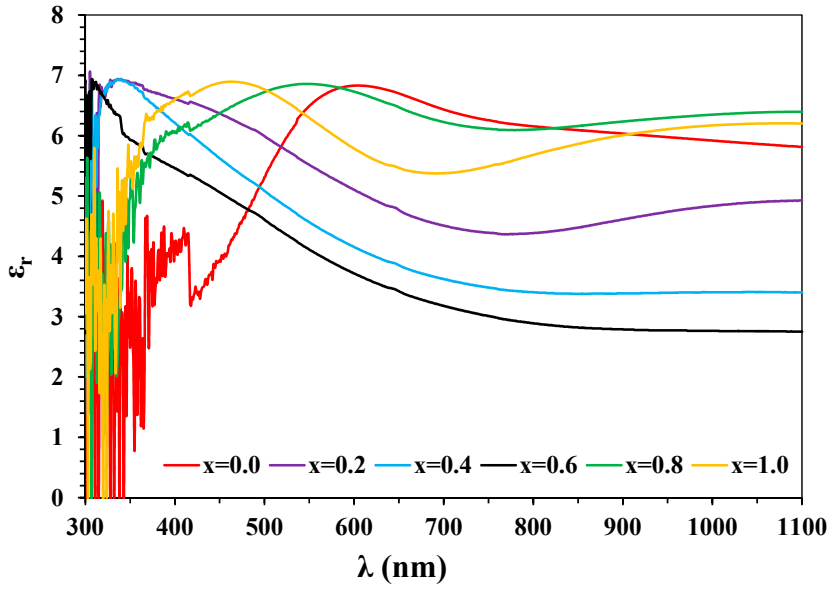

Figure 11: Variation of the real part of the dielectric function (ε_r) with wavelength (λ) for $Cu_2ZnSn(S_{1-x}Se_x)_4$ nanostructures thin films with x = 0.0, 0.2, 0.4, 0.6, 0.8 and 1.0.

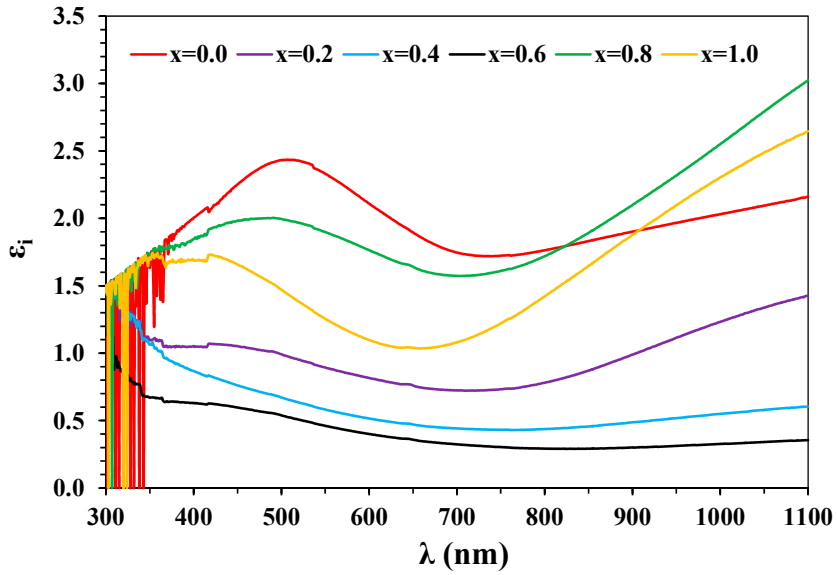

Figure 12: Variation of the real part of the dielectric function (ε_i) with wavelength (λ) for $Cu_2ZnSn(S_{1-x}Se_x)_4$ nanostructures thin films with x = 0.0, 0.2, 0.4, 0.6, 0.8 and 1.0.

The n and ε_r are the parameters used to characterise the propagation trend of light. Usually, n is known as the relation between the velocity of light in a vacuum and the velocity in a medium. Thus, the ε_r gives data about the n behaviour in the medium, i.e., the way that the material is capable of decelerating the passage of incident light. The k depicts the way the material can absorb incident light, which is related to the ε_i. The k depicts the rate of amplitude attenuation of the incident electromagnetic wave due to absorption by the specific medium. Thus, a higher value of ε_r indicates a higher value of n, and hence high bending or slowing of the incident light will occur after passing the medium, while a higher value of ε_i means high light absorption through the medium, which is very important for photovoltaic solar cells. In general, the ε_r and ε_i give information about how light interacts with $Cu_2ZnSn(S_{1-x}Se_x)_4$. The pronounced increase in surface roughness at x = 0.6 is associated with a transitional structural regime between amorphous and crystalline phases. While increased roughness can enhance optical scattering and light trapping, the simultaneous reduction in grain size leads to a higher density of grain boundaries, which may promote carrier recombination. The observed variations in dielectric loss (ε_i) suggest that defect-related absorption plays a more dominant role than pure light trapping. Therefore, the optical response at x = 0.6 likely results from a competition between enhanced scattering and increased recombination losses.

While this manuscript focuses on optical characterizations, the reported refractive index, extinction coefficient, and dielectric responses provide insights into the electronic structure and optical transitions of the films. Variations in ε_r and ε_i correlate with changes in band structure and defect-related absorption, suggesting differences in charge generation and possible recombination pathways. However, optical constants alone cannot directly quantify charge transport parameters such as carrier concentration, mobility, or resistivity. The observed improvements in structural crystallinity and optical absorption (higher k, optimized n) are projected to enhance charge carrier generation and mobility, ultimately boosting J_{sc} and V_{oc}. Based on findings from solar energy materials and solar cells, these optical improvements, combined with reduced structural defects, correlate directly with lower recombination rates and improved charge transport efficiency.

Previous studies have demonstrated that extracting transport parameters requires dedicated electrical techniques such as Hall effect or conductivity measurements, as optical responses reflect electronic structure but do not uniquely determine electrical transport properties. Therefore, we acknowledge that comprehensive electrical characterization is necessary to fully assess the photovoltaic performance and efficiency of the studied films, and future work will include such measurements to correlate optical properties with actual device metrics [37].

Table 4 presents the values of the optical parameters and the E_g at a wavelength of 550 nm for $Cu_2ZnSn(S_{1-x}Se_x)_4$ nanostructures thin films.

4 Conclusions

Developing a better nanostructured CZTSSe thin film for efficient photovoltaic solar cell applications was the goal of this work. By using the melt technique and quenching, the semiconductor $Cu_2ZnSn(S_{1-x}Se_x)_4$ nanostructure was created. Using the pulsed laser deposition approach, a thin coating of the $Cu_2ZnSn(S_{1-x}Se_x)_4$ nanostructure was applied on Corning glass. The following specifics of the thin film's structural and optical characteristics have been examined:

- Basic structural and optical characterizations (such as XRD, AFM, and UV-Vis-NI spectroscopy) validated the quality of the deposited thin films.
- The crystal orientations (112), (200), (220), and (312) were shown by the XRD peaks.
- The XRD analysis conclusively confirmed the presence of a mixed kesterite–stannite crystal structure with a preferred (112) orientation in the $Cu_2ZnSn(S_{1-x}Se_x)_4$ films. By raising the Se concentration from 0.0 to 0.6, the optical constants collectively decreased.
- An increase in Se content resulted in a widening of the energy band gap, attaining its maximum at $x = 0.6$.
- In solar cell and optoelectronic material applications, the optimal band gap energy value for the thin film absorber material is lower than the obtained energy gap of $Cu_2ZnSnSe_4$.
- Nanostructured $Cu_2ZnSn(S_{1-x}Se_x)_4$ films are promising absorber layers for solar cell applications.

Acknowledgement: Not applicable.

Funding Statement: The authors received no specific funding for this study.

Author Contributions: Bushra A. Hasan: writing—original draft, visualization, methodology, investigation, formal analysis, data curation. Ameer J. Fadhl: writing—review & editing, validation, investigation, formal analysis, data curation. Ahmad A. Hasan: writing—original draft, validation, methodology, investigation. Yasser A. Jebbar: writing—review & editing, Resources. All authors reviewed and approved the final version of the manuscript.

Availability of Data and Materials: Data will be made available on request.

Ethics Approval: Not applicable.

Conflicts of Interest: The authors declare no conflicts of interest.

References

1. Todorov T, Mitzi DB. Direct liquid coating of chalcopyrite light-absorbing layers for photovoltaic devices. Eur J Inorg Chem. 2010;2010(1):17–28. [CrossRef].
2. Chirilă A, Buecheler S, Pianezzi F, Bloesch P, Gretener C, Uhl AR, et al. Highly efficient Cu(In,Ga)Se_2 solar cells grown on flexible polymer films. Nat Mater. 2011;10(11):857–61. [CrossRef].

3. Turnley JW, Agrawal R. Solution processed metal chalcogenide semiconductors for inorganic thin film photovoltaics. Chem Commun. 2024;60(40):5245–69. [CrossRef].
4. Repins I, Contreras MA, Egaas B, DeHart C, Scharf J, Perkins CL, et al. 19.9% efficient ZnO/CdS/CuInGaSe^2 solar cell with 81.2% fill factor. Prog Photovolt Res Appl. 2008;16(3):235–9. [CrossRef].
5. Jackson P, Hariskos D, Lotter E, Paetel S, Wuerz R, Menner R, et al. New world record efficiency for Cu(In,Ga)Se_2 thin-film solar cells beyond 20%. Prog Photovolt Res Appl. 2011;19(7):894–7. [CrossRef].
6. Guo Q, Ford GM, Agrawal R, Hillhouse HW. Ink formulation and low-temperature incorporation of sodium to yield 12% efficient Cu(In,Ga)$(S,Se)_2$ solar cells from sulfide nanocrystal inks. Prog Photovolt Res Appl. 2013;21(1):64–71. [CrossRef].
7. Redinger A, Berg DM, Dale PJ, Siebentritt S. The consequences of kesterite equilibria for efficient solar cells. J Am Chem Soc. 2011;133(10):3320–3. [CrossRef].
8. Li JB, Chawla V, Clemens BM. Investigating the role of grain boundaries in CZTS and CZTSSe thin film solar cells with scanning probe microscopy. Adv Mater. 2012;24(6):720–3. [CrossRef].
9. Scragg JJ, Watjen JT, Edoff M, Ericson T, Kubart T, Platzer-Bjorkman C. A detrimental reaction at the molybdenum back contact in $Cu_2ZnSn(S,Se)_4$ thin-film solar cells. J Am Chem Soc. 2012;134(47):19330–3. [CrossRef].
10. Wang L, Ban J, Han L, Zhou Z, Zhou W, Kou D, et al. Defects in kesterite materials towards high-efficiency solar cells: Origin, impact, characterization, and engineering. J Mater Chem A. 2024;12(38):25643–77. [CrossRef].
11. Ahmed S, Reuter KB, Gunawan O, Guo L, Romankiw LT, Deligianni H. A high efficiency electrodeposited Cu_2ZnSnS_4 solar cell. Adv Energy Mater. 2012;2(2):253–9. [CrossRef].
12. Cao Y, Denny MS Jr, Caspar JV, Farneth WE, Guo Q, Ionkin AS, et al. High-efficiency solution-processed $Cu_2ZnSn(S,Se)_4$ thin-film solar cells prepared from binary and ternary nanoparticles. J Am Chem Soc. 2012;134(38):15644–7. [CrossRef].
13. Shin B, Gunawan O, Zhu Y, Bojarczuk NA, Chey SJ, Guha S. Thin film solar cell with 8.4% power conversion efficiency using an earth-abundant Cu_2ZnSnS_4 absorber. Prog Photovolt Res Appl. 2013;21(1):72–6. [CrossRef].
14. Scragg JJ, Ericson T, Fontané X, Izquierdo-Roca V, Pérez-Rodríguez A, Kubart T, et al. Rapid annealing of reactively sputtered precursors for Cu_2ZnSnS_4 solar cells. Prog Photovolt Res Appl. 2014;22(1):10–7. [CrossRef].
15. Habas SE, Platt HA, van Hest MF, Ginley DS. Low-cost inorganic solar cells: From ink to printed device. Chem Rev. 2010;110(11):6571–94. [CrossRef].
16. Woo K, Kim Y, Moon J. A non-toxic, solution-processed, earth abundant absorbing layer for thin-film solar cells. Energy Environ Sci. 2012;5(1):5340–5. [CrossRef].
17. Hasan BA, Umran DA, Mankoshi MAK, editors. Characterization of CuInSTe/CdS heterojunctions. J Phys Conf Ser. 2018;1032:012020. [CrossRef].
18. Hasan BA. Electrical properties of $AgSb(S_xSe_{1-x})_2$ thin films. J Phys Conf Ser. 2019;1279:012049. [CrossRef].
19. Heavens OS. Optical properties of thin solid films. New York, NY, USA: Dover Publications; 1991.
20. Gesing TM, Robben L. Determination of the average crystallite size and the crystallite size distribution: The envelope function approach (EnvACS). J Appl Crystallogr. 2024;57(5):1466–76. [CrossRef].
21. Nematov D, Kholmurodov K, Stanchik A, Fayzullaev K, Gnatovskaya V, Kudzoev T. On the optical properties of the $Cu_2ZnSn\ [S_{1-x}Se_x]_4$ system in the IR range. Trends Sci. 2023;20(2):4058. [CrossRef].
22. Ramirez EA, Gordillo G. Study of optical and structural properties of CZTS thin films grown by co-evaporation and spray pyrolysis. J Phys Conf Ser. 2016;687:012041. [CrossRef].
23. El-Khozondar HJ, El-Khozondar RJ, Sahmoud AN, Nassar YF. Performance investigation of multilayer-layers solar cell based in ZnS-CZTSSe. Solar Energy. 2025;291:113410. [CrossRef].
24. Stanchik AV, Tivanov MS, Tyukhov II, Juskenas R, Korolik OV, Gremenok VF, et al. Temperature dependence of Raman scattering in $Cu_2ZnSnSe_4$ thin films on a Ta foil substrate. Sol Energy. 2020;201:480–8. [CrossRef].
25. Siebentritt S, Schorr S. Kesterites—A challenging material for solar cells. Prog Photovolt Res Appl. 2012;20:512–9. [CrossRef].
26. Niu C, Zhu T, Lv Y. Influence of surface morphology on absorptivity of light-absorbing materials. Int J Photoenergy. 2019;2019:1476217. [CrossRef].
27. Zhang Y, Sun Y. Investigation of S/Se ratio on the properties of solution-processed CZTSSe solar cell. Chalcogenide Lett. 2016;13(9):397–402.

28. Kişnişci Z, Özel F, Tuğluoğlu N, Yüksel ÖF. Structural and optical properties of $Cu_2ZnSnSe_4$ nanocrystals thin film. Opt Quantum Electron. 2024;56:1239. [CrossRef].
29. El-Alamassi DM, El-Khozondar HJ, Shabat M. Efficiency enhancement of solar cell using metamaterials. Int J Nano Stud Technol. 2015;4(2):84–7. [CrossRef].
30. Benmazouza B, Sahraoui T, Adnane M, Hamamousse N, Djelloul A, Larbah Y, et al. Inexpensive optimized Cu_2ZnSnS_4 absorption layer elaborated with a homemade SILAR method. J Nano Electron Phys. 2023;15(2):02004. [CrossRef].
31. Hasan BA, Mahmood SS, Issa HH, Issa TT. Structural, morphology and optical properties of AlxSb1-x thin films prepared by Pulsed laser deposition (PLD). AIP Conf Proc. 2021;2372(1):040010. [CrossRef].
32. Hasan BA, Kadhim MA, editors. Structure, morphology and optical properties of thermally evaporated Cu_2S thin films annealed at different temperatures. AIP Conf Proc. 2019;2144(1):030021. [CrossRef].
33. Hasan AA, Mohammed AA. Optical and A.C. electrical properties of PMMA/CB, PMMA/G and PMMA/(CB+G) composites. Dig J Nanomater Biostruct. 2020;15(3):923–30. [CrossRef].
34. Ebnalwaled AA, Sadek AH, Ismail SH, Mohamed GG. Structural, optical, dielectric, and surface properties of polyimide hybrid nanocomposites films embedded mesoporous silica nanoparticles synthesized from rice husk ash for optoelectronic applications. Opt Quantum Electron. 2022; 54(11):690. [CrossRef].
35. Hasan AA, Abbas YM, Ibraheem FT, Hasan BA. Optical and gas sensor properties of PAN:PPy:Gr nanocomposites. Iraqi J Appl Phys. 2024;20(2A):245–53.
36. Hasan BA, Issa HH, Hasan AA. Fabrication and investigation of structural, optical and dielectric properties of ZnO:MnO_2 composites. Iraqi J Appl Phys. 2023;19(4A):21–8.
37. Hassan AH, Khan YC, Wang YC. Drift-diffusion modeling-guided interface optimization in $BaHfS_3$ chalcogenide perovskite solar cells. Sol Energy Mater Sol Cells. 2025;294:113889. [CrossRef].